Physics of Plasmas ARTICLE scitation.org/journal/php

Screening of resonant magnetic perturbation fields assuming various plasma flow models

Cite as: Phys. Plasmas **28**, 082504 (2021); doi: 10.1063/5.0057338
Submitted: 19 May 2021 · Accepted: 22 July 2021 ·
Published Online: 4 August 2021

View Online Export Citation CrossMark

L. Li,[1,2,a)] Y. Q. Liu,[3] G. L. Xia,[4] Y. F. Wang,[1,2] Q. B. Luan,[5] W. D. Zhang,[5] and F. C. Zhong[1,2]

AFFILIATIONS

[1]College of Science, Donghua University, Shanghai 201620, China
[2]Member of Magnetic Confinement Fusion Research Centre, Ministry of Education, Shanghai 201620, China
[3]General Atomics, P.O. Box 85608, San Diego, California 92186-5608, USA
[4]CCFE, Culham Science Centre, Abingdon OX14 3DB, United Kingdom of Great Britain and Northern Ireland
[5]Faculty of Electronic information and Electrical Engineering, Dalian University of Technology, Dalian 116024, China

[a)]Author to whom correspondence should be addressed: lili8068@dhu.edu.cn

ABSTRACT

A recently updated version of the MARS-F code [Y. Q. Liu *et al.*, Phys. Plasmas **7**, 3681 (2000); L. Li *et al.*, Phys. Plasmas **25**, 082512 (2018); and G. L. Xia *et al.*, Nucl. Fusion **59**, 126035 (2019)] is utilized to numerically investigate the plasma screening effect on the applied resonant magnetic perturbation (RMP) field, assuming various equilibrium flow models, including the toroidal flow, the parallel flow and their combinations, and poloidal and toroidal projections of the parallel flow. A parallel equilibrium flow with a uniform radial profile is found to have no effect on plasma screening of the RMP field. A sheared parallel flow, however, does change plasma screening. The poloidal projection of the parallel flow weakens plasma screening in the resistive-inertial regime. The effect on the favorable average curvature regime is found, however, to be non-monotonic. With the increasing flow speed, the poloidal projection first weakens Glasser-Green-Johnson (GGJ)-screening. Further increase in the flow speed results in enhanced GGJ-screening again. This non-monotonic behavior is related to the perturbed parallel shielding current, which appears also off the mode rational surface at fast flow due to additional resonances between the RMP perturbation and the sound wave continuum. These results indicate that flow induced plasma screening to the RMP field can have complicated characteristics, which, in turn, can have implications on the RMP field penetration into the plasma in experiments for controlling the edge localized modes.

I. INTRODUCTION

Screening of the external resonant magnetic perturbation (RMP) fields, due to plasma response, plays an important role in 3D physics processes in tokamak plasmas, including the resonant field amplification (RFA),[1–5] the mode locking,[6,7] the error field correction[8–10] as well as control of magneto-hydrodynamic (MHD) instabilities, such as the resistive wall mode[11–14] and the edge localized modes (ELMs).[15–21] In particular, it has been realized that the non-linear field penetration can offer a critical understanding of the type-I ELM suppression by RMP fields.[22] Plasma screening is one of the two key physics components involved in the resonant field penetration dynamics, with the other being the plasma flow.

It is well known in theory that, in a resistive plasma, screening of the external RMP field originates from the plasma conductivity and plasma flow.[23–25] Extensive computational modeling efforts have been devoted to investigate the plasma response induced screening,[26–35] in the context of RMP and with particular emphasis on the role played by the toroidal plasma flow. In the context of two-fluid formulation, the role of the perpendicular electron flow has also been studied.[36,37]

The mostly studied plasma screening, within the single fluid formulation, is that associated with the toroidal plasma rotation. Two types of screening regimes with the toroidal flow have been previously identified[38,39] and are illustrated in Fig. 1 below as a typical example. Plotted here is the ratio of the $n = 1$ (n is the toroidal harmonic number of the applied perturbation field) total resonant field amplitude (including both the vacuum field and the plasma response) to the corresponding vacuum component, while scanning the toroidal plasma rotation frequency Ω_0. The dimensionless radial field is defined as

$$b^1 = \frac{q}{R_0^2 B_0}\left(\frac{\mathbf{b}\cdot\nabla\psi}{\mathbf{B}\cdot\nabla\phi}\right),$$

where q is the safety factor, $\mathbf{b}$ and $\mathbf{B}$ are the perturbed and equilibrium magnetic fields, respectively, R_0 is the major radius of the torus, B_0 is the vacuum toroidal field on the magnetic axis, ϕ is the

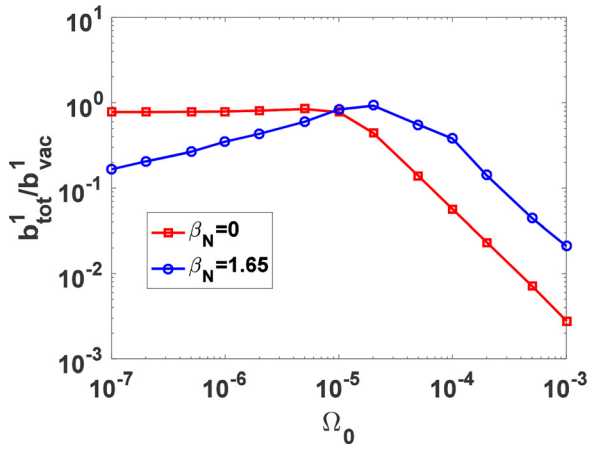

FIG. 1. Illustration of the toroidal favorable curvature induced plasma screening (blue curve) at slow toroidal plasma rotation and with finite equilibrium pressure ($\beta_N = 1.65$), and the lack of it (red curve) with vanishing pressure ($\beta_N = 0$). The screening changes to the resistive-inertial regime at fast toroidal rotation. Assumed is an equilibrium with circular plasma cross section and with a single resonant surface inside the plasma for the $n = 1$ perturbation. Plotted is the amplitude of the $m/n = 2/1$ total resonant radial field perturbation amplitude normalized by the corresponding vacuum field. The toroidal rotation frequency Ω_0 is normalized by the toroidal Alfvén frequency, and b^1 is the radial component of the perturbed magnetic field $\mathbf{b}$, where b^1_{vac} and b^1_{tot} are the one with the vacuum field and total field (including the plasma response). The Lundquist number is chosen at $S = 10^9$. β_N here is a normalized beta value of $\beta_N = \beta a B_0/I_P$, where β is the ratio of the volume averaged plasma pressure to the magnetic pressure and a, B_0, I_P are the minor radius of the plasma boundary, the vacuum toroidal field at the magnetic axis, and total plasma current, respectively.

geometric toroidal angle, and ψ is the equilibrium poloidal magnetic flux.

A uniform toroidal rotation is assumed here along the plasma minor radius. The blue curve in Fig. 1 shows both the so-called Glasser-Green-Johnson (GGJ) screening regime[38–40] at very slow toroidal plasma rotation and the resistive-inertial (RI) regime[23] at faster flow. The GGJ-screening regime is associated with the favorable average curvature effect in a toroidal magnetic geometry,[41] which occurs in the presence of finite equilibrium pressure (more precisely finite pressure gradient) at the mode resonant surface. In this regime, the plasma response, in terms of the total resonant field amplitude, decreases with the decreasing plasma flow speed. The GGI-screening effect disappears when the plasma equilibrium pressure vanishes (red curve in Fig. 1). A more conventional is the resistive-inertial screening regime, where the plasma response is reduced at the increasing flow speed. This screening effect occurs independent of the plasma pressure.

In this work, we shall consider a range of fundamental physics aspects of plasma screening due to other types of equilibrium flow, namely, the poloidal and parallel flows. In particular, we shall investigate how these flows affect the aforementioned screening regimes within the single fluid model. The study is partly motivated by the following observations.

(i) Fast poloidal flow has been measured in tokamak experiments, especially in the plasma core region with the formation of the internal transport barrier[42,43] as well as in the plasma edge region in many experiments.[44–46]

(ii) Poloidal and parallel plasma flows have been found to affect MHD instabilities, such as the resistive wall mode.[47,48] An interesting finding from Ref. 48 is that parallel plasma flow merely introduces a rotational transform along the equilibrium magnetic field lines, without providing a direct stabilization to the mode. On the other hand, parallel flow can affect the mode stability via the poloidally or toroidally projected component. It is, therefore, interesting to understand how the parallel (and poloidal) flow affects the plasma screening.

(iii) In a recent study,[49] it was found that the large RMP field induced magnetic field line ergodization in an ITER plasma produces an appreciable plasma flow along the magnetic field lines.

We point out that the plasma density profile plays a special role when the parallel equilibrium flow is introduced, since the equilibrium mass conservation condition implies that the parallel flow is coupled to the plasma density. In most of our study, we shall assume a uniform density profile. However, a comparative study will also be made where we assume a sheared density profile. We also mention that, in most cases, we consider the additional screening effect, introduced by the parallel or poloidal flow, on top of that produced by an existing toroidal flow. Plasma screening due to a pure parallel/poloidal flow is treated as the limiting case when the toroidal flow vanishes. A reason for taking this approach will be elaborated later on.

We emphasize that this study aims at investigating the fundamental and often subtle physics associated with flow screening. Practical aspects, e.g., how large a role the poloidal or parallel flow can play in the in realistic experiments, are not the focus of the present work. For this reason, we shall consider a simple (but toroidal) plasma equilibrium. We shall also treat the parallel/poloidal flow speed as a free parameter and scan the amplitude.

Section II briefly describes the equilibrium and the plasma flow models that we adopt in this study. Section III reports the screening effect by the poloidal flow (on top of a uniform toroidal flow). Section IV reports a similar systematic study but assuming the parallel flow. The role of the (non-uniform) plasma density profile is discussed in Sec. V. Section VI summarizes the work.

II. EQUILIBRIUM AND PLASAMA FLOW MODELS

In this work, the plasma response to the external RMP field is computed by the upgraded MARS-F code, which implemented the parallel equilibrium flow in perturbed single fluid MHD equations.[48] The new implementation, combined with an earlier update of incorporating poloidally varying toroidal flow in MARS-F,[40] enables separate consideration of the screening effect of the poloidal equilibrium flow, as will be explained in this section. The full computational model of the upgraded MARS-F code is described in Appendix A.

As mentioned before, we assume a simple equilibrium with the aspect ratio of 10 and a circular poloidal cross section. The radial profiles of the equilibrium safety factor q and pressure are shown in Fig. 2. The equilibrium density profile, not shown here, is assumed uniform if not indicated otherwise. Note that the safety factor is chosen such that only one rational surface ($q = 2$) is present inside the plasma for the $n = 1$ perturbation. We mention that the same equilibrium has been adopted in previous work.[38–40] The plasma response shown in Fig. 1 is also based on this equilibrium.

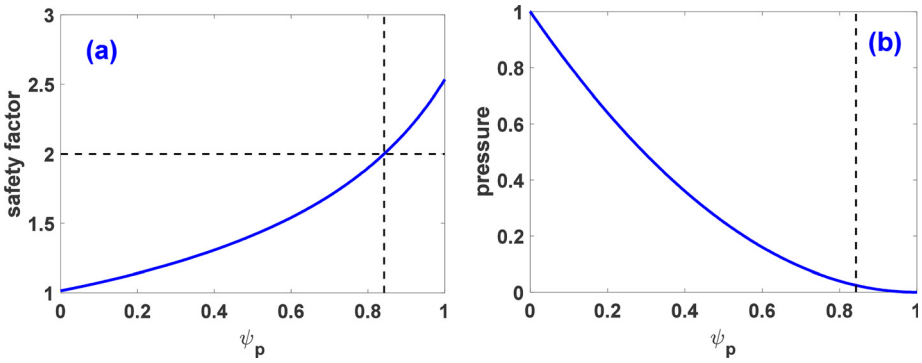

FIG. 2. The radial profiles of (a) the safety factor and (b) the plasma pressure, for a Wesson-like equilibrium with the parabolic current density profile. Note that plotted in (b) is the pressure profile normalized to unit at the magnetic axis. The pressure amplitude is tuned to obtain different β_N values. The vertical dashed lines indicate the location of the $q = 2$ rational surface.

In the following study, we shall consider various combinations of the equilibrium flow components, based on a generic implementation as described in Appendix A. More specifically, we shall compare the screening effect due to five equilibrium flow models listed below. The first ($\mathbf{V}_1$) is a pure toroidal flow

$$\mathbf{V}_1(s) = \Omega(s)\mathbf{e}_\phi, \tag{1}$$

where $\Omega(s)$ is the angular frequency of the toroidal rotation and $\mathbf{e}_\phi = R^2\nabla\phi$ is the contravariant basis vector along the geometric toroidal angle ϕ. The illustrative results shown in Fig. 1 are obtained with this flow model, where $\Omega(s) = \Omega_0$ is uniform along the plasma minor radius s.

The next flow model is a pure poloidal flow $\mathbf{V}_2$, which is the poloidal projection of the mass-conserving parallel equilibrium flow

$$\mathbf{V}_2(s) = \left[U(s)\psi'/\rho\mathcal{J}\right]\mathbf{e}_\chi, \tag{2}$$

where $\mathbf{e}_\chi = \mathcal{J}\nabla\phi \times \nabla s$ is the covariant basis vector along the poloidal angle χ. $U(s)$ specifies the parallel flow velocity, which varies only along the plasma minor radius. $\psi' = \partial\psi/\partial s$ is the radial derivative of the equilibrium poloidal flux function along the plasma minor radius s, the plasma equilibrium density ρ, and the Jacobian, $\mathcal{J}$, associated with the curve-linear toroidal coordinate system (s, χ, ϕ). A more generic flow model $\mathbf{V}_3$ is obtained by combining $\mathbf{V}_1$ and $\mathbf{V}_2$

$$\mathbf{V}_3(s) = \left[U(s)\psi'/\rho\mathcal{J}\right]\mathbf{e}_\chi + \Omega(s)\mathbf{e}_\phi. \tag{3}$$

Next, a pure parallel equilibrium plasma flow ($\mathbf{V}_4$) that conserves the plasma mass, i.e., $\nabla\cdot(\rho\mathbf{V}_4) = 0$, can be written as

$$\mathbf{V}_4(s) = \left[U(s)/\rho\right]\mathbf{B} = \left[U(s)\psi'/\rho\mathcal{J}\right]\mathbf{e}_\chi + \left[FU(s)/\rho R^2(s,\chi)\right]\mathbf{e}_\phi, \tag{4}$$

where F is the equilibrium poloidal current flux function and R is the major radius. Finally, the most generic equilibrium flow model $\mathbf{V}_5$ is obtained by combining the parallel flow $\mathbf{V}_4$ with the pure toroidal flow $\mathbf{V}_1$,

$$\mathbf{V}_5(s) = \left[U(s)/\rho\right]\mathbf{B} + \Omega(s)\mathbf{e}_\phi. \tag{5}$$

We point out that, by construction, all the above five flow models satisfy the equilibrium mass conservation condition. For the poloidal flow, in particular, this is achieved because we do not choose an arbitrary form but specifically the poloidal projection of the parallel flow. On the other hand, keeping the pure poloidal flow $\mathbf{V}_2$ alone creates certain degeneracy in the plasma response model, thus resulting in numerical challenges with MARS-F computations. This peculiar degeneracy is analyzed in Appendix B 1. We find that the best way of numerically recovering plasma screening due to a pure poloidal flow is to add a small amount of toroidal flow (i.e., $\mathbf{V}_3$), thus letting the latter approaches zero. At small values of toroidal flow, careful tuning of the radial mesh (which is highly packed near the mode rational surface) is often required in order to obtain numerically converged results.

Finally, we mention that, in this work, the toroidal rotation frequency $\Omega(s)$ is always normalized by the toroidal Alfvén frequency. The parallel velocity component $U(s)$ has a unit of neither linear nor angular velocity. $U(s)$ is in fact normalized by a factor $v_A\rho_0/B_0$ in this work, where v_A is the toroidal Alfvén speed, ρ_0 is the on-axis plasma mass density, and B_0 is the on-axis vacuum toroidal field.

III. SCREENING OF RMP FIELDS DUE TO THE POLOIDAL PLASMA FLOW

In this section, we consider the plasma flow model $\mathbf{V}_3$ as defined by Eq. (3). Both the toroidal and parallel velocity components are assumed uniform, i.e., $\Omega(s) = \Omega_0$ and $U(s) = U_0$. As explained before, the screening effect due to the pure poloidal flow $\mathbf{V}_2$ is obtained as the limiting case of vanishing Ω_0. The numerical results are summarized in Fig. 3, where we scan Ω_0 while fixing U_0 at different values. At $U_0 = 0$, we recover toroidal flow screening results with the flow model of $\mathbf{V}_1$, as reported in Fig. 1.

Several interesting points can be made based on Fig. 3. First, the presence of finite poloidal flow somewhat reduces GGJ-screening at slow toroidal flow. As a result, the screening effect does not depend on the toroidal rotation frequency speed Ω_0 [Fig. 3(a)] nor the sign of Ω_0 [Fig. 3(b)], as the latter approaches zero and the poloidal flow, meanwhile, remains finite. This is because the GGJ-term inversely scales with the perturbation frequency, and either poloidal or toroidal flow induces finite perturbation frequency, which weakens the GGJ-term. The reduction is non-monotonic though, as will be more clearly demonstrated later on. Second, the poloidal flow also affects plasma screening in the RI-regime, i.e., at faster toroidal flow. Finally, the presence of poloidal flow generates an intermediate region in Ω_0, where a sharp reduction in the resonant field amplitude (i.e., strong screening) is observed. We note that these sharp peaks are not numerical artifacts, since they are robustly obtained by tuning numerical parameters, such as the radial mesh packing. In what follows, we shall closely examine each of these three screening regimes.

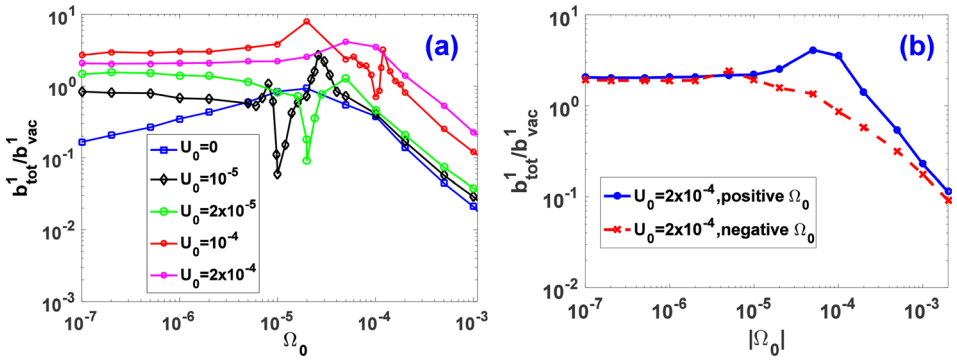

FIG. 3. Screening of the $n = 1$ resonant magnetic field due to the poloidal plasma flow. Assumed is the flow model $\mathbf{V}_3$. The effect of pure poloidal flow $\mathbf{V}_2$ is obtained at the limit of vanishing toroidal rotation frequency Ω_0. Plotted is the amplitude of the $m/n = 2/1$ total resonant radial field perturbation amplitude normalized by the corresponding vacuum field, assuming (a) positive toroidal flow with varying poloidal flow speed and (b) fixed poloidal flow of $U_0 = 2 \times 10^{-4}$ but with either positive (blue solid line) or negative (red dashed line) toroidal flow. The Lundquist number is chosen at $S = 10^9$. The plasma equilibrium pressure is $\beta_N = 1.65$.

A. Effect of poloidal flow on the GGJ-screening regime

Here, we scan the parallel flow velocity U_0 while fixing Ω_0 at 10^{-6}. This choice of a small value for the toroidal rotation frequency ensures that we are in the GGJ-screening regime. We emphasize that, although the parallel flow velocity U_0 is scanned, only the poloidal projection of the latter is included here, since we are assuming the flow model $\mathbf{V}_3$.

Figure 4 summarizes the computational results. It is interesting to note that, in the GGJ-regime, the screening effect due to the poloidal flow is not monotonic: The screening effect is first weakened by the slow poloidal flow and then enhanced with further increasing U_0 [Fig. 4(a)]. In other words, the phenomenology of resonant field screening by the poloidal flow is similar to that by the toroidal flow. This non-monotonic change in the screening behavior is closely related to the perturbed parallel current generated inside the plasma, near the $q = 2$ resonant surface as shown in Figs. 4(b)–4(d). In both the small (2×10^{-5}) and large (2×10^{-4}) limits of U_0, a large parallel current at the $q = 2$ surface provides the screening effect. In the fast poloidal flow case with $U_0 = 2 \times 10^{-4}$ [Fig. 4(d)], two additional peaks appear in the perturbed parallel current, located roughly

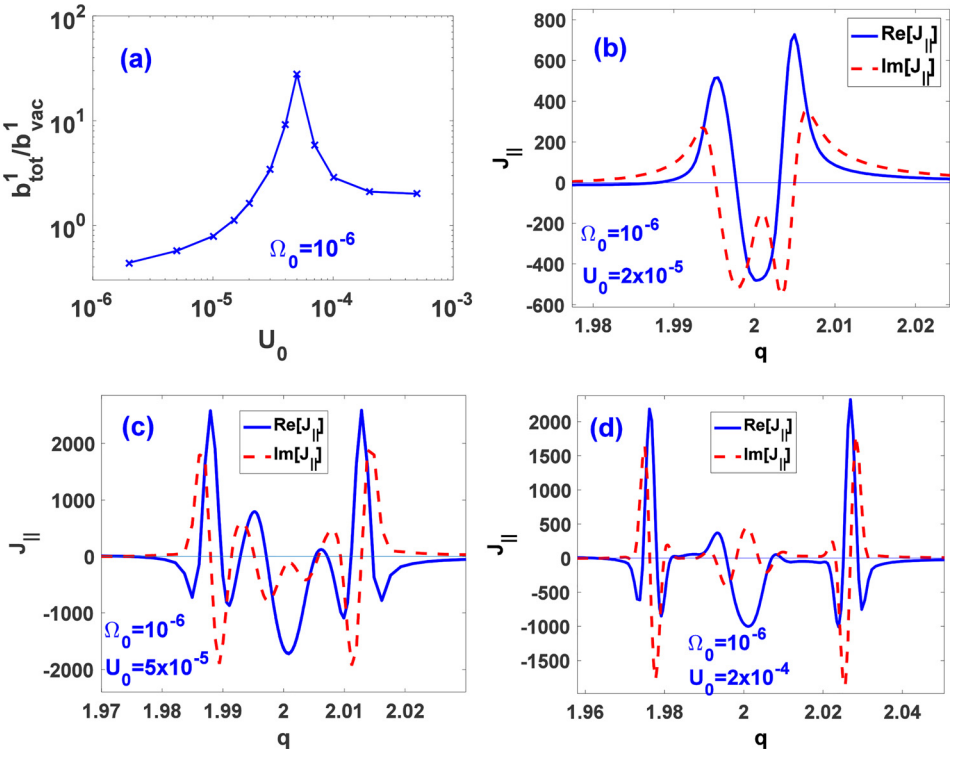

FIG. 4. Screening effect due to the poloidal flow in the GGJ-regime. Assumed is the plasma flow model $\mathbf{V}_3$ with a small (and fixed) toroidal rotation frequency $\Omega_0 = 10^{-6}$. Plotted in (a) is the amplitude of the $m/n = 2/1$ total resonant radial field perturbation amplitude normalized by the corresponding vacuum field, while scanning U_0. Plotted in (b), (c), and (d) are the real (solid) and imaginary (dashed) parts of the $m/n = 2/1$ perturbed plasma parallel current near the $q = 2$ rational surface, at fixed $U_0 = 2 \times 10^{-5}$, $U_0 = 5 \times 10^{-5}$, and $U_0 = 2 \times 10^{-4}$. The Lundquist number is chosen at $S = 10^9$. The plasma equilibrium pressure is $\beta_N = 1.65$.

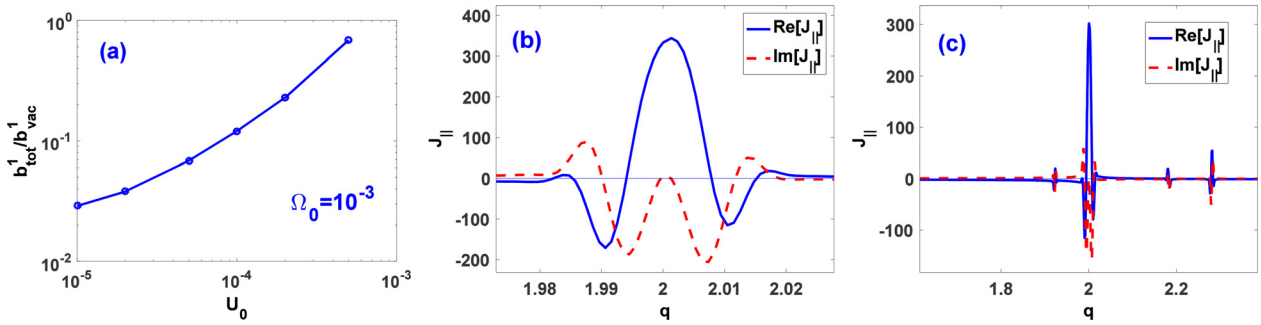

FIG. 5. Screening effect due to poloidal flow in the RI-regime. Assumed is the plasma flow model $\mathbf{V}_3$ with a fixed toroidal rotation frequency of $\Omega_0 = 10^{-3}$. Plotted in (a) is the amplitude of the $m/n = 2/1$ total resonant radial field perturbation amplitude normalized by the corresponding vacuum field, while scanning U_0. Plotted in (b) and (c) are the real (solid) and imaginary (dashed) parts of the $m/n = 2/1$ perturbed plasma parallel current near the $q = 2$ rational surface, at fixed $U_0 = 2 \times 10^{-5}$ and $U_0 = 2 \times 10^{-4}$, respectively. The Lundquist number is chosen at $S = 10^9$. The plasma equilibrium pressure is $\beta_N = 1.65$.

symmetrically off the $q = 2$ rational surface. These two peaks are due to the resonances between the perturbation field and the continuum sound waves (Appendixes B 2 and B 3).

B. Effect of poloidal flow on the RI-screening regime

Next, we scan U_0 at the fixed toroidal rotation frequency of $\Omega_0 = 10^{-3}$, again assuming the plasma flow model $\mathbf{V}_3$. The results, reported in Fig. 5, show that increasing poloidal flow speed monotonically weakens plasma screening in the RI-regime [Fig. 5(a)]. This can again be understood by comparing the perturbed parallel current for two cases with slow ($U_0 = 2 \times 10^{-5}$) and fast ($U_0 = 2 \times 10^{-4}$) poloidal flow, shown in Figs. 5(b) and 5(c), respectively. In both cases, the fundamental screening is provided by the perturbed current near the $q = 2$ surface. However, additional current perturbations occur off the $q = 2$ rational surface with faster poloidal flow [Fig. 5(c)], due to continuum sound wave resonances. These additional parallel current peaks tend to partially compensate the fundamental screening provided by the current sheet near the $q = 2$ surface, leading to the overall weakened screening of the resonant field perturbation.

We point out that those sharp perturbed current peaks from Fig. 5(c) are numerically well resolved by MARS-F. This is illustrated by the enlarged version reported in Fig. 6, where each current peak is shown in a separate plot. Note the similarity of the fundamental

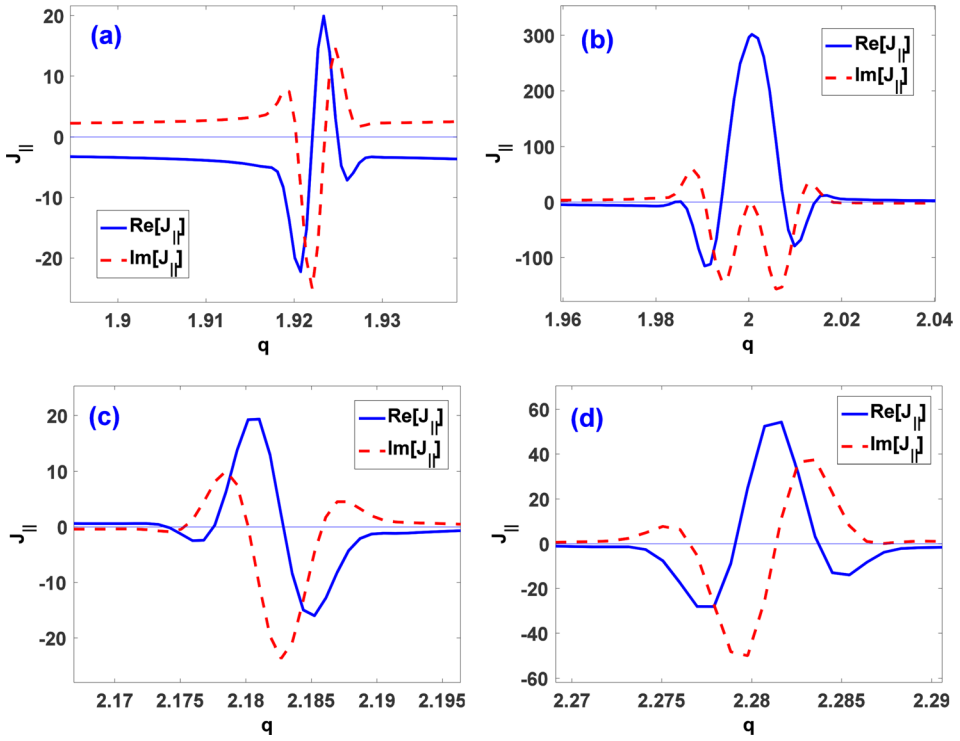

FIG. 6. Detailed distribution of the real (solid) and imaginary (dashed) parts of the $m/n = 2/1$ perturbed parallel current at four peaking location shown in Fig. 5(c), where (a) near $q = 1.92$, (b) near $q = 2$, (c) near $q = 2.18$, and (d) near $q = 2.28$. Assumed is the plasma flow model $\mathbf{V}_3$ with $\Omega_0 = 10^{-3}$ and $U_0 = 2 \times 10^{-4}$. The Lundquist number is chosen at $S = 10^9$. The plasma equilibrium pressure is $\beta_N = 1.65$.

shielding current pattern near the $q = 2$ surface, between Figs. 6(b) and 5(b). Note also the difference in symmetry, in terms of the radial distribution of the perturbed current, between the fundamental shielding current [Fig. 6(b)] and those produced by sound wave resonances [Figs. 6(a), 6(c), and 6(d)]. Such a difference has been previously noticed in the context of toroidal flow induced plasma screening.[41]

C. Effect of poloidal flow on the intermediate regime between GGJ- and RI-screening

Figure 3 shows that poloidal flow plays a different role in the intermediate region between the GGJ- and the RI-screening regimes. In particular, sharp peaks appear, indicating strong screening with certain combinations of the poloidal and toroidal flows. In what follows, we try to understand the physics nature of these peaks, by looking closely into one example near $\Omega_0 = 10^{-4}$.

Figure 7(a) plots the computed resonant field screening factor while scanning U_0 (with the flow model $\mathbf{V_3}$). We note a strongly non-monotonic behavior of the screening factor vs the poloidal flow speed at the finite plasma pressure of $\beta_N = 1.65$ (curve in blue). For comparison, a smooth monotonic decay of the screening factor is computed for the case of vanishing equilibrium pressure of $\beta_N = 0$ (curve in red). The non-monotonic behavior of the finite-pressure case, in particular, the sharp enhancement of the plasma screening at $U_0 > 10^{-4}$, is again associated with the continuum wave resonances due to the poloidal plasma flow. These continuum wave resonances introduce multiple resonant surfaces off the $q = 2$ rational surface (Appendixes B 2 and B 3). An extreme example is shown in Fig. 7(b) at the poloidal flow of $U_0 = 9 \times 10^{-4}$. The multiple peaks in the

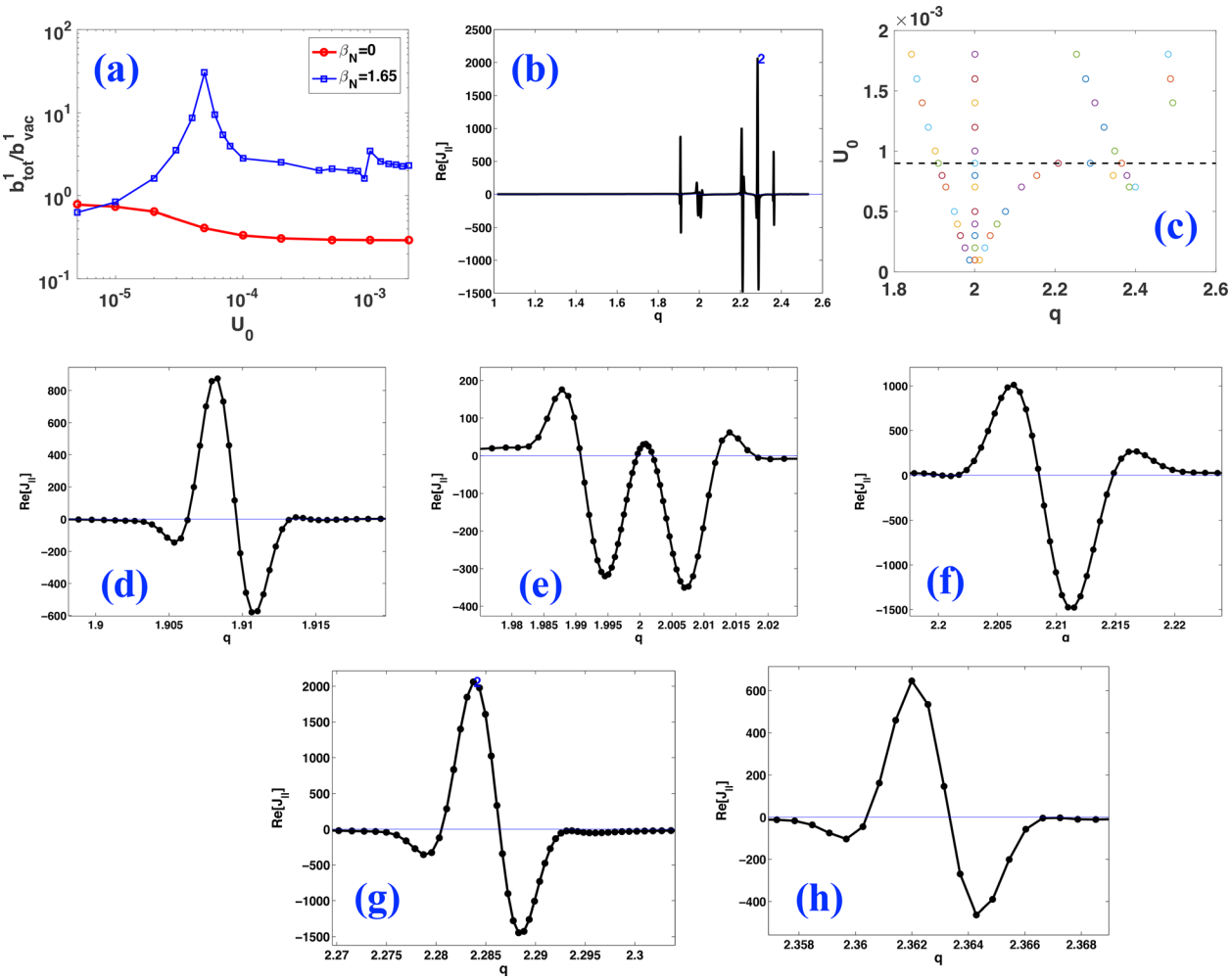

FIG. 7. Screening effect due to poloidal flow in the intermediate region between the GGJ- and the RI-regimes. Assumed is the plasma flow model $\mathbf{V}_3$ with a fixed toroidal rotation frequency of $\Omega_0 = 10^{-4}$: (a) the amplitude of the $m/n = 2/1$ total resonant radial field perturbation amplitude normalized by the corresponding vacuum field, while scanning U_0, (b) the real part of the $m/n = 2/1$ perturbed plasma parallel current at $U_0 = 9 \times 10^{-4}$, (c) the radial location (in terms of q-values) of multiple resonant surfaces with increasing U_0, [(d)–(h)] zoom-in version of the radial profile of the perturbed parallel current shown in (b) but near each resonant surface. The Lundquist number is chosen at $S = 10^9$. The plasma equilibrium pressure is $\beta_N = 1.65$ in [(b)–(h)] as well as for the blue curve in (a), and $\beta_N = 0$ for the red curve in (a).

computed perturbed parallel current density, which are all numerically well resolved as shown in Figs. 7(d)–7(h), are due to resonances between the applied resonant perturbation and the shear Alfvén and sound waves in the plasma. In particular, the Alfvén continuum resonance creates a symmetric parallel current distribution around the $q=2$ surface [Fig. 7(e)], while the sound wave continuum resonances create four peaked asymmetric current distribution further away from the $q=2$ surface [Figs. 7(d), 7(f), 7(g), and 7(h)].

The radial location of the aforementioned resonant surfaces varies with the poloidal flow speed, measured here by U_0. Indeed, Fig. 7(c) shows a gradual splitting of these resonant surface (away from the $q=2$ surface) as we increase U_0. Note that additional resonant surfaces also appear at certain finite U_0 (e.g., $U_0 \sim 6\times10^{-4}$). This is due to the existence of multiple roots of the sound wave resonant conditions as derived in Appendix B.

IV. SCREENING OF RMP FIELDS DUE TO PARALLEL PLASMA FLOW

In what follows, we investigate the effect of parallel equilibrium flow on the plasma screening of the resonant field component, by applying the flow model $\mathbf{V}_5$. The pure parallel flow $\mathbf{V}_4$ is recovered as a limiting case of $\mathbf{V}_5$ at vanishing Ω. The key results are summarized in Fig. 8. Figure 8(a) shows that the parallel flow does not induce additional screening compared to that due to the toroidal flow $\mathbf{V}_1$. This is further confirmed by Fig. 8(b), where we vary the ratio of U_0/Ω_0 at different (fixed) values of the toroidal rotation frequency Ω_0. The plasma screening factor remains constant (within numerical accuracy) while scanning the parallel flow speed. Examination of the perturbed parallel current in the plasma further confirms that a uniform parallel flow almost does not affect the plasma response in both screening regimes, as shown in Figs. 8(c) and 8(d). Figures 8(c) and 8(d) show the results for the real part of the perturbed current, and similar results are obtained when comparing the imaginary part.

An insight into the above result is obtained from Ref. 48, where it has been proposed that the parallel equilibrium flow essentially introduces a transformation of the reference frame along the (equilibrium) magnetic field lines, without modifying the fundamental underlining physics. As a consequence, the parallel flow was found to have no effect on the resistive wall mode stability in Ref. 48. In this work, we also establish that a uniform parallel flow does not affect plasma screening. We emphasize that this numerical finding has no rigorous analytic explanation yet. The resonant condition (B16) from Appendix B 3 is derived with too simplified assumptions to explain this interesting screening regime. On the other hand, we have shown in Sec. III that the poloidal projection of the parallel flow does affect plasma screening (in particular, via introduction of multiple peaks in the shielding current off the $q=2$ surface, due to continuum wave resonances). This implies that the screening effect, introduced by the poloidal and toroidal projections of the parallel flow, cancels each other.

Note that, since we have so far assumed uniform radial profiles for both the parallel flow component $U(s)$ and the plasma density $\rho(s)$, the aforementioned transformation of the reference frame along the magnetic field lines, due to the parallel flow, is global. It remains a question of whether the similar conclusion still holds, if the transformation is local, in other words, if the parallel flow component $U(s)$ or the plasma density $\rho(s)$ has a finite shearing rate from one flux surface to the other. Part of the purpose of Sec. V is to answer this question, by assuming the sheared plasma density profile.

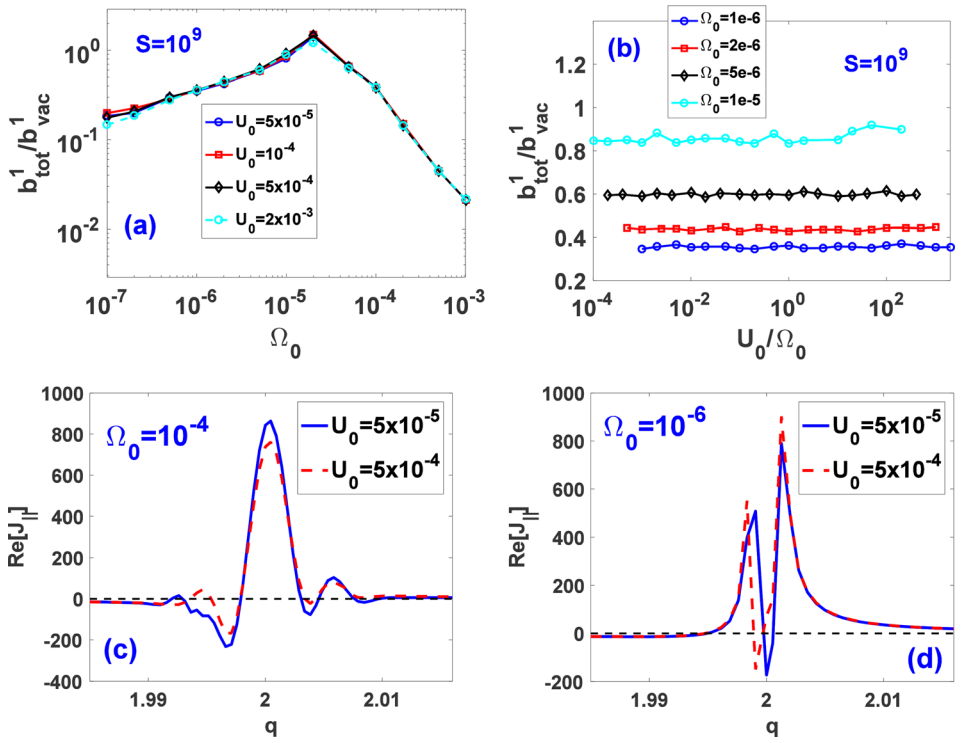

FIG. 8. Screening effect due to the parallel plasma flow in both the GGJ- and the RI-regimes. Assumed is the plasma flow model $\mathbf{V}_5$ with (a) varying toroidal rotation frequency Ω_0 at different values of parallel speed U_0, and (b) varying the ratio U_0/Ω_0 at different values of Ω_0. Plotted is the amplitude of the $m/n=2/1$ total resonant radial field perturbation amplitude normalized by the corresponding vacuum field. Plots [(c) and (d)] compare the real part of the $m/n=2/1$ perturbed parallel current density near the $q=2$ rational surface between $U_0=5\times10^{-5}$ and $U_0=5\times10^{-4}$, in either (c) the RI-regime ($\Omega_0=10^{-4}$) or (d) the GGI-regime ($\Omega_0=10^{-6}$). The Lundquist number is chosen at $S=10^9$. The plasma equilibrium pressure is $\beta_N=1.65$.

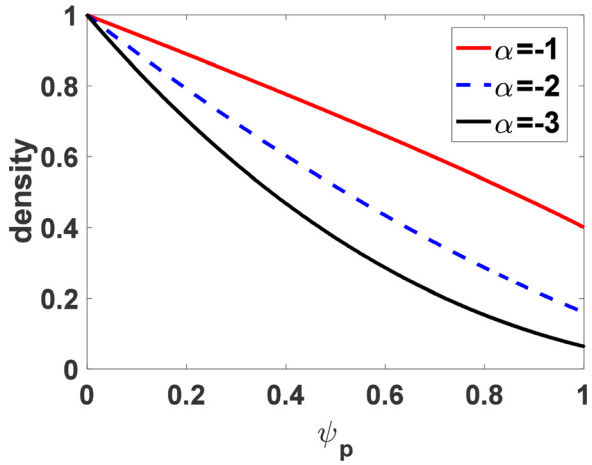

FIG. 9. Radial profiles of the plasma equilibrium density with varying shear, controlled by the shaping parameter α as defined in Eq. (6). Here, the plasma density has been normalized by the density at the magnetic axis.

V. SCREENING OF RMP FIELDS WITH THE SHEARED PLASMA DENSITY PROFILE

Since the parallel flow model $\mathbf{V}_4$ always involves the combination of $U(s)/\rho(s)$ [cf. Eq. (4)], we shall assume sheared plasma density profiles while keeping the parallel flow component constant, $U(s) = U_0$. A family of density profiles is defined based on the safety factor q-profile with different choices of the shaping factor α,

$$\rho(s) = \left[q(s)/q(s=0)\right]^{\alpha}. \tag{6}$$

Note that the above density profile is normalized to unity at the magnetic axis, as in the MARS-F formulation. There is no particular physics reason for using the safety factor profile to define the density profile, beside the fact that, with $\alpha < 0$, Eq. (6) yields monotonically decaying density along the plasma minor radius, which is normally the case in tokamak plasmas. Figure 9 plots three density profiles, with $\alpha = -1, -2, -3$, respectively, which we shall use in the following study. We shall investigate the influence of the profile shear with both flow models $\mathbf{V}_3$ and $\mathbf{V}_5$.

A. Plasma screening with the flow model $\mathbf{V}_3$ and sheared density profile

In this sub-section, we focus on the density shear effect on the GGJ- and RI-screening regimes, in the presence of poloidal projection of the parallel flow. Figure 10 shows that the plasma screening generally depends on the density profile shear and equivalently on the shear of the parallel flow velocity. In the GGJ-regime [Fig. 10(a)], increasing the density profile shear shifts the peak (corresponding to the least screening) of the plasma response field amplitude toward the smaller value of U_0. The plasma screening is, however, not much affected by the density shear in the two limiting cases of small and large U_0.

On the other hand, the presence of (larger) density profile shear monotonically reduces the plasma screening in the RI-regime, provided by the poloidal projection of the parallel flow [Fig. 10(b)]. Although not shown here, we observe similar resonances with plasma continuum waves due to the poloidal flow to that reported in Sec. III with the uniform density profile. Furthermore, the resonant splitting, i.e., the location of multiple peaks of the perturbed parallel current along the plasma minor radius, depends on the density profile shear as expected.

B. Plasma screening with the flow model $\mathbf{V}_5$ and sheared density profile

Figure 8 shows that a radially uniform parallel flow does not affect the plasma screening due to a *global* transformation of the reference frame along magnetic field lines. The transformation becomes *local* with a sheared parallel flow or equivalently with a sheared plasma density profile. Figure 11 shows that the latter does affect the plasma screening. Here, we fix $U_0 = 5 \times 10^{-5}$ and scan the toroidal rotation frequency, assuming the plasma flow model $\mathbf{V}_5$. The computed screening factor with different density profiles (Fig. 9) is compared in Fig. 11(a), showing significant modifications to the result with the uniform density profile ($\alpha = 0$) for both the GGJ- and RE-regimes. The effect is somewhat stronger for the GGJ-regime. Furthermore,

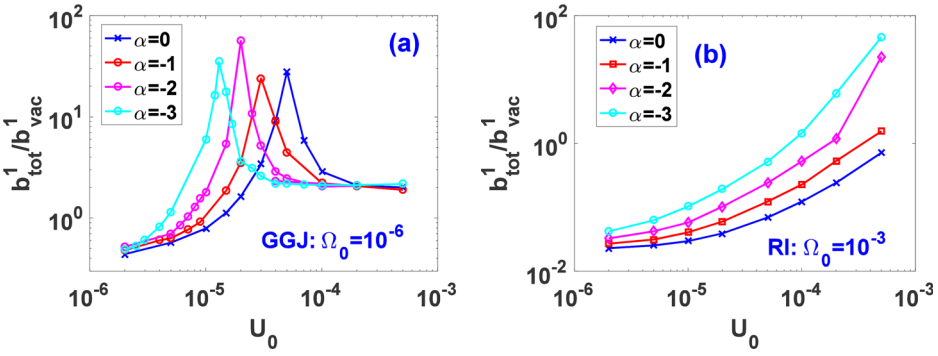

FIG. 10. Influence of the plasma density profile shearing on the plasma screening due to poloidal flow, in (a) the GGJ- and (b) the RI-screening regimes, respectively. The density profile is controlled by the shaping parameter α and shown in Fig. 9, with $\alpha = 0$ corresponding to a uniform profile. Assumed is the plasma flow model $\mathbf{V}_3$ with (a) $\Omega_0 = 10^{-6}$ and (b) $\Omega_0 = 10^{-3}$. Plotted is the amplitude of the $m/n = 2/1$ total resonant radial field perturbation amplitude normalized by the corresponding vacuum field. The Lundquist number is chosen at $S = 10^9$. The plasma equilibrium pressure is $\beta_N = 1.65$.

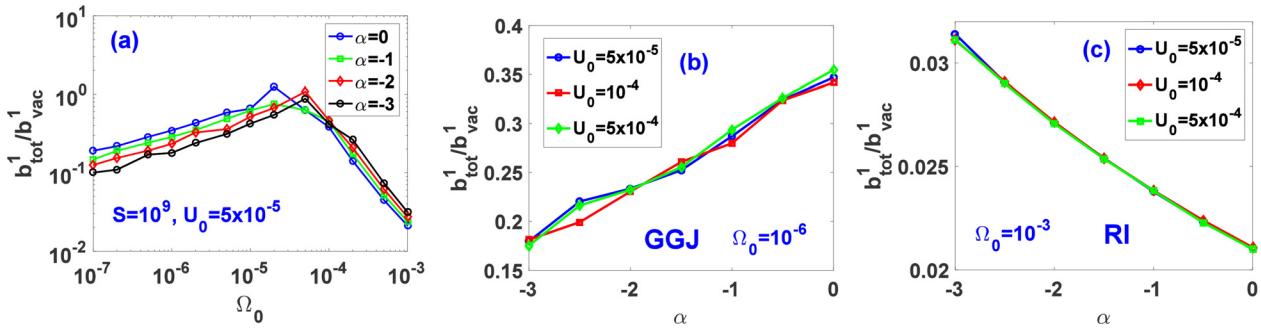

FIG. 11. Influence of plasma density profile shearing on screening due to the parallel flow. The density profile is controlled by the shaping parameter α, with $\alpha = 0$ corresponding to a uniform profile. Assumed is the plasma flow model $\mathbf{V}_5$. Plotted is the amplitude of the $m/n = 2/1$ total resonant radial field perturbation amplitude normalized by the corresponding vacuum field, while (a) varying toroidal rotation frequency Ω_0, (b) varying the shaping parameter α at different values of the parallel speed U_0 and fixed the toroidal rotation frequency in the GGJ-regime $\Omega_0 = 10^{-6}$, and (c) fixed the toroidal rotation frequency in the RI-regime $\Omega_0 = 10^{-3}$. The Lundquist number is chosen at $S = 10^9$. The plasma equilibrium pressure is $\beta_N = 1.65$.

increasing the density profile shear enhances GGJ-screening ($\Omega_0 = 10^{-6}$) [Fig. 11(b)] but weakens RI-screening ($\Omega_0 = 10^{-3}$) [Fig. 11(c)]. This holds for various choices of the parallel flow speed and is not sensitive to the latter, indicating that the effect mainly comes from the shear of $U(s)/\rho(s)$, not the amplitude.

VI. CONCLUSION AND DISCUSSION

Utilizing a recently updated MARS-F code, we investigate the plasma screening effect on the applied resonant magnetic perturbation field assuming various equilibrium flow models, including the toroidal flow, the parallel flow and their combinations, and the poloidal and toroidal projections of the parallel flow. The 2/1 tearing mode response is used as an example to illustrate different screening regimes.

We find that a parallel equilibrium flow, with a uniform radial profile for $U(s)/\rho(s)$, does not affect the plasma screening of the RMP field. This is because such a uniform flow merely introduces a global rotational transform along equilibrium magnetic field lines. On the other hand, any factor that violates this global nature will lead to (parallel) flow modification of plasma screening. One possibility is to keep a uniform $U(s) = const$ while introducing finite shear to the plasma density profile $\rho(s)$. With a monotonically decreasing density profile, which is a typical case in tokamak plasmas, we find that the parallel equilibrium flow enhances the GGJ-screening but weakens the RI-screening. The screening factor is found to be roughly linearly scaled with the density profile shaping factor α.

The poloidal projection of the parallel flow also weakens the RI-screening. The effect on the GGJ-screening, however, is non-monotonic. With the increasing flow speed, the poloidal projection first weakens the GGJ-screening. Further increase in the flow speed results in enhanced GGJ-screening again. We explain this non-monotonic behavior in terms of the radial structure of the perturbed parallel current, which provides shielding to the resonant radial field perturbation. At faster poloidal equilibrium flow, new shielding currents appear off the mode rational surface, due to additional resonances between the RMP perturbation and the sound wave continuum.

These results indicate that the flow induced plasma screening to the RMP field can have complicated characteristics, which, in turn, can have implications on the RMP field penetration into the plasma during ELM control experiments. The eventual screening factor depends on the plasma toroidal flow regimes (e.g., GGJ- vs RI-regimes) and the combination of different flow components. On the other hand, we emphasize that the results are obtained within the single-fluid model. It is known that the flow regime changes with the inclusion of the two-fluid effect. Investigation of the parallel flow, and its poloidal or toroidal projection, on the plasma screening within the two-fluid theory represents an important future work.

Associated with the GGJ-screening are also other physics effects that we ignored in this study. For instance, additional thermal transport[50] or the presence of large magnetic islands[51] was found to effectively eliminate the GGJ-screening. It is, therefore, interesting to understand how these additional physics effects can change the plasma screening in the presence of parallel flow or its projections. A recent work[52] finds that the any physics effect that alters the parallel sound wave dynamics will also affect the GGJ-regime. Since the parallel flow also participates into the resonance with parallel sound waves, as identified in this study, we expect certain synergistic effects between parallel flow and many other physics (e.g., the parallel viscosity induced wave damping) in determining the plasma screening in the GGJ-regime.

The equilibrium that we assume in this work is for a simple large aspect ratio plasma with L-mode like profiles. The physics mechanisms exploited here, e.g., the GGJ-effect, the sound wave, and Alfvén wave continuum resonances due to the plasma response to a static RMP field, however, also apply to more realistic equilibria (H-mode plasma, conventional or low aspect ratio, strong plasma shaping, etc.) from experiments. The MARS-F code is capable of capturing these physics effects as demonstrated, e.g., in Refs. 53 and 54 Investigating various flow options on the plasma screening to the RMP field for realistic experiments is, therefore, a useful work that we will pursue in future.

ACKNOWLEDGMENTS

This work was funded by Fundamental Research Funds for the Central Universities [Grant No. 2232021G-10], National Natural Science Foundation of China (NSFC) [Grant Nos. 12075053, 11505021, and 11975068], and National Key R&D Program of China under Contract Nos. 2017YFE030052, 2017YFE0301100,

2017YFE0301104, 2017YFE0300500 and 2017YFE0300501. The work was also supported by the U.S. DoE Office of Science under Contract Nos. DE-FG02-95ER54309 and DEFC02-04ER54698. This report was prepared as an account of work sponsored by an agency of the United States Government. Neither the United States Government nor any agency thereof, nor any of their employees, makes any warranty, express, or implied, or assumes any legal liability or responsibility for the accuracy, completeness, or usefulness of any information, apparatus, product, or process disclosed, or represents that its use would not infringe privately owned rights. Reference herein to any specific commercial product, process, or service by trade name, trademark, manufacturer, or otherwise, does not necessarily constitute or imply its endorsement, recommendation, or favoring by the United States Government or any agency thereof. The views and opinions of authors expressed herein do not necessarily state or reflect those of the United States Government or any agency thereof. The views and opinions expressed herein do not necessarily reflect those of the European Commission.

APPENDIX A: COMPUTATIONAL MODEL IN MARS-F WITH THE PARALLEL EQUILIBRIUM FLOW

Below we show the full set of single fluid, linearized resistive MHD equations for plasma response modeling in generic toroidal geometry, including both equilibrium toroidal and parallel flows, i.e., the flow model $\mathbf{V}_5$ described by Eq. (5),

$$\rho_1 = -\nabla\cdot(\rho\boldsymbol{\xi}), \tag{A1}$$

$$(i\omega_{RMP}+in\Omega)\boldsymbol{\xi} = \mathbf{v} + (\boldsymbol{\xi}\cdot\nabla\Omega)R^2\nabla\phi - \rho^{-1}U\nabla\times(\boldsymbol{\xi}\times\mathbf{B}) + \rho^{-2}U\rho_1\mathbf{B} + (\boldsymbol{\xi}\cdot\nabla U)\rho^{-1}\mathbf{B}, \tag{A2}$$

$$\rho(i\omega_{RMP}+in\Omega)\mathbf{v} = -\nabla p + \mathbf{j}\times\mathbf{B} + \mathbf{J}\times\mathbf{b} + \rho\left[2\Omega\hat{\mathbf{Z}}\times\mathbf{v} - (\mathbf{v}\cdot\nabla\Omega)R^2\nabla\phi\right] - U\nabla(\mathbf{v}\cdot\mathbf{B}) + U\mathbf{v}\times\mathbf{J} + U\mathbf{B}\times(\nabla\times\mathbf{v}) - \mathbf{B}[\rho\nabla(\rho^{-1}U)\cdot\mathbf{v}], \tag{A3}$$

$$(i\omega_{RMP}+in\Omega)\mathbf{b} = \nabla\times(\mathbf{v}\times\mathbf{B}) + (\mathbf{b}\cdot\nabla\Omega)R^2\nabla\phi - \nabla\times(\eta\mathbf{j}) - \nabla\times\left(\rho^{-1}U\mathbf{b}\times\mathbf{B}\right), \tag{A4}$$

$$p = -\boldsymbol{\xi}\cdot\nabla P - \Gamma P\nabla\cdot\boldsymbol{\xi}, \tag{A5}$$

$$\mathbf{j} = \nabla\times\mathbf{b}, \tag{A6}$$

where the variables ρ_1, $\boldsymbol{\xi}$, $\mathbf{v}$, $\mathbf{b}$, $\mathbf{j}$, and p denote the plasma perturbed density, displacement, velocity, magnetic field, current, and pressure, respectively. All the perturbed quantities depend on the toroidal angle ϕ in the analytic form of $\exp(in\phi)$, where n is the toroidal mode number. The equilibrium plasma density, magnetic field, current, and pressure are denoted by ρ, $\mathbf{B}$, $\mathbf{J}$, and P, respectively. Ω and U denote the toroidal and parallel components of the equilibrium flow. ω_{RMP} is the frequency of the applied external RMP field, with $\omega_{RMP}=0$ for a static RMP field produced by the dc coil current as assumed in this work. The RMP coil current density $\mathbf{j}_{\mathrm{RMP}}$ is treated as a source term and included in the model via Ampère's law $\mathbf{j}_{\mathrm{RMP}} = \nabla\times\mathbf{b}$. The other quantities shown in above equations are the ratio of specific heats $\Gamma = 5/3$, with the unit vector of the vertical direction $\hat{\mathbf{Z}}$ and the plasma resistivity η. As evident from the above equations, the presence of a finite equilibrium parallel flow introduces several additional terms to perturbed momentum balance equation (A3) and induction equation (A4).

APPENDIX B: SOME ANALYTIC CONSIDERATIONS IN THE PRESENCE OF EQUILIBRIUM FLOW

In what follows, we examine a numerical problem associated with purely parallel equilibrium flow, when computing the plasma response to a dc external RMP field. The resonant phenomena with continuum sound waves, as observed in MARS-F modeling, will also be discussed.

In a generic toroidal geometry with the equilibrium magnetic flux surface based coordinate system (s, χ, ϕ) as defined in MARS-F, the plasma displacement and the perturbed fluid velocity can be represented as $\boldsymbol{\xi} = \xi^1\mathbf{a}_1 + \xi^2\mathbf{a}_2 + \xi^3\mathbf{a}_3$ and $\mathbf{v} = v^1\mathbf{a}_1 + v^2\mathbf{a}_2 + v^3\mathbf{a}_3$, respectively. The basis vectors are defined as $\mathbf{a}_1 = \left(\frac{\mathbf{B}}{B}\times\mathbf{e}_s\right)\times\frac{\mathbf{B}}{B}$, $\mathbf{a}_2 = \mathcal{J}\frac{\mathbf{B}\times\nabla s}{B^2}$, and $\mathbf{a}_3 = \mathbf{B}$. Here, $\mathbf{B}$ is the equilibrium magnetic field, $\mathbf{e}_s = \mathcal{J}\nabla\chi\times\nabla\phi$ is the covariant basis vector along the radial coordinate s, and $\mathcal{J} = (\nabla s\cdot\nabla\chi\times\nabla\phi)^{-1} = \mathbf{a}_1\cdot\mathbf{a}_2\times\mathbf{a}_3$ is the Jacobian associated with the curvilinear coordinates. We consider the parallel sound wave propagation physics associated with MHD equations (A1)–(A6), projected along the aforementioned basis vectors

$$(i\omega_{RMP}+in\Omega)\xi^1 = v^1 - \frac{U}{\rho}\left(\frac{\psi'}{\mathcal{J}}\frac{\partial\xi^1}{\partial\chi} + \frac{F}{R^2}\frac{\partial\xi^1}{\partial\phi}\right), \tag{B1}$$

$$\rho(i\omega_{RMP}+in\Omega)\mathcal{J}B^2v^3 = -\psi'\frac{\partial p}{\partial\chi} - \frac{\mathcal{J}F}{R^2}\frac{\partial p}{\partial\phi} - U\left[\psi'\frac{\partial(B^2v^3)}{\partial\chi} + \frac{\mathcal{J}F}{R^2}\frac{\partial(B^2v^3)}{\partial\phi}\right], \tag{B2}$$

$$(i\omega_{RMP}+in\Omega)\mathcal{J}p = -\Gamma P\left[\frac{\partial}{\partial\chi}(\psi'v^3) + \frac{\partial}{\partial\phi}\left(\frac{\mathcal{J}F}{R^2}v^3\right)\right] - \mathcal{J}\rho^{-1}U\mathbf{B}\cdot\nabla p. \tag{B3}$$

Note that only terms responsible for the parallel sound wave propagation are retained in above Eqs. (B2) and (B3). In a PEST-like straight-field-line coordinate system (with the proper choice of the poloidal angle χ), we have the global safety factor calculated as $q = JF/(\psi'R^2)$. With Fourier representations along both the poloidal and toroidal angles, we have $\frac{\partial}{\partial\chi}\to im$ and $\frac{\partial}{\partial\phi}\to -in$. Taking into account the above relations and ignoring the certain toroidal coupling effect, Eqs. (B1)–(B3) can be written as

$$(i\omega_{RMP}+in\Omega)\xi^1 = v^1 - \frac{U}{\rho\mathcal{J}}\psi'(m-nq)\xi^1, \tag{B4}$$

$$\rho(i\omega_{RMP}+in\Omega)\mathcal{J}B^2v^3 = -i\psi'(m-nq)(P+UB^2v^3), \tag{B5}$$

$$(i\omega_{RMP}+in\Omega)\mathcal{J}p = -\Gamma Pi\psi'(m-nq)v^3 - \mathcal{J}\rho^{-1}U\mathbf{B}\cdot\nabla p. \tag{B6}$$

1. A singularity issue associated with the parallel flow with vanishing toroidal flow

This corresponds to the equilibrium flow model $\mathbf{V}_4$ defined by Eq. (4). With the vanishing toroidal equilibrium flow ($\Omega = 0$) and

considering a dc RMP field ($\omega_{RMP} = 0$), Eq. (B4) relates the radial plasma displacement to the perturbed radial velocity

$$\mathcal{J}v^1 = -\frac{U}{\rho}\psi'(m - nq)\xi^1. \tag{B7}$$

Evidently, Eq. (B7) introduces a new singularity into the MHD equations, as compared to the case with the vanishing equilibrium parallel flow. This singularity is resolved either by enforcing a vanishing perturbed radial velocity at mode rational surfaces or by introducing a small but finite equilibrium toroidal flow Ω (or equivalently by considering an ac RMP field). We emphasize that in the special case of $\Omega = U = \omega_{RMP} = 0$, Eq. (B4) has degeneracy. The plasma radial displacement is un-determined in this case.

The fundamental reason for the appearance of the singularity issue in Eq. (B7) is our simplified model assumption for the plasma density $\rho = \rho(s)$. In a proper equilibrium with the generic plasma flow, the plasma density should be 2D function of (s, χ), which, in turn, introduces toroidal coupling in Eq. (B7), which then resolves the singularity issue at mode rational surfaces. In our study, we choose to have a small but finite toroidal equilibrium flow (i.e., flow models $\mathbf{V}_3$ and $\mathbf{V}_5$) to avoid this issue.

2. Continuum resonance with sound waves: Pure toroidal flow

We now focus on the parallel sound wave resonances described by Eqs. (B5) and (B6). We first consider the case with the vanishing equilibrium parallel flow, $U = 0$. Equations (B5) and (B6) are simplified to

$$\rho(i\omega_{RMP} + in\Omega)\mathcal{J}B^2v^3 = -i\psi'(m - nq)p, \tag{B8}$$

$$(i\omega_{RMP} + in\Omega)\mathcal{J}p = -\Gamma P i\psi'(m - nq)v^3. \tag{B9}$$

By combining the above two equations, we have

$$(i\omega_{RMP} + in\Omega)^2v^3 = -\left[V_s(m - nq)\frac{\psi'}{\mathcal{J}B}\right]^2 v^3, \tag{B10}$$

where $V_s = \sqrt{\Gamma P/\rho}$. Again assuming a dc RMP, we have

$$n^2\Omega^2 = \omega_S^2, \tag{B11}$$

where $\omega_S \simeq k_\parallel V_s$ is the sound wave frequency and $k_\parallel \equiv \frac{m-nq}{qR}$. Equation (B11), thus, illustrates the well-known resonance condition between the perturbed field and the sound wave continuum, which is typically satisfied near (but off) the mode rational surfaces. Note that a resonance condition with shear Alfvén waves can be identified in an analogous manner, where the parallel sound wave frequency from the right-hand side of Eq. (B11) is replaced by the parallel shear Alfvén frequency. Next, we derive a similar resonance condition but in the presence of a parallel equilibrium flow.

3. Continuum resonance with sound waves: Parallel flow

With the generic plasma flow model $\mathbf{V}_5$, Eqs. (B5) and (B6) can be re-written as

$$\rho(i\omega_{RMP} + in\Omega)Bv^3 = -ik_\parallel(P + UB^2v^3), \tag{B12}$$

$$(i\omega_{RMP} + in\Omega)p = -ik_\parallel B\left(\Gamma Pv^3 + \rho^{-1}UP\right). \tag{B13}$$

Assuming $\omega_{RMP} = 0$ and denoting $\rho^{-1}UB \equiv U_\parallel$ and $Bv^3 \equiv \hat{v}^3$, we have

$$\left(n\Omega + U_\parallel k_\parallel\right)\hat{v}^3 = -k_\parallel\rho^{-1}P, \tag{B14}$$

$$\left(n\Omega + k_\parallel U_\parallel\right)p = -k_\parallel\Gamma P\hat{v}^3. \tag{B15}$$

Combining Eqs. (B14) and (B15) yields the continuum sound wave resonance condition in the presence of parallel equilibrium flow

$$\left(n\Omega + k_\parallel U_\parallel\right)^2 = \omega_S^2. \tag{B16}$$

This kind of resonance is responsible for the appearance of multiple resonant surfaces as shown in Figs. 5 and 7.

DATA AVAILABILITY

The data that support the findings of this study are available from the corresponding author upon reasonable request.

REFERENCES

[1]H. Boozer, Phys. Rev. Lett. **86**, 5059 (2001).
[2]Y. Q. Liu, Plasma Phys. Controlled Fusion **48**, 969 (2006).
[3]M. J. Lanctot, H. Reimerdes, A. M. Garofalo, M. S. Chu, Y. Q. Liu, E. J. Strait, G. L. Jackson, R. J. La Haye, M. Okabayashi, T. H. Osborne, and M. J. Schaffer, Phys. Plasmas **17**, 030701 (2010).
[4]M. J. Lanctot, H. Reimerdes, A. M. Garofalo, M. S. Chu, J. M. Hanson, Y. Q. Liu, G. A. Navratil, I. N. Bogatu, Y. In, G. L. Jackson, R. J. La Haye, M. Okayabashi, J.-K. Park, M. J. Schaffer, O. Schmitz, E. J. Strait, and A. D. Turnbull, Phys. Plasmas **18**, 056121 (2011).
[5]Z. R. Wang, M. J. Lanctot, Y. Q. Liu, J.-K. Park, and J. E. Menard, Phys. Rev. Lett. **114**, 145005 (2015).
[6]R. Fitzpatrick and T. C. Hender, Phys. Fluids B: Plasma Phys. **3**, 644 (1991).
[7]R. Fitzpatrick and E. P. Yu, Phys. Plasmas **5**, 2340 (1998).
[8]R. J. Buttery, M. De' Benedetti, D. A. Gates, Yu. Gribov, T. C. Hender, R. J. La Haye, P. Leahy, J. A. Leuer, A. W. Morris, A. Santagiustina, J. T. Scoville, B. J. D. Tubbing, JET Team, COMPASS-D Research Team, and DIII-D Team, Nucl. Fusion **39**, 1827 (1999).
[9]J.-K. Park, M. J. Schaffer, R. J. La Haye, T. J. Scoville, and J. E. Menard, Nucl. Fusion **51**, 023003 (2011).
[10]Y. Q. Liu, A. Kirk, A. J. Thornton, and MAST Team, Plasma Phys. Controlled Fusion **56**, 104002 (2014).
[11]A. Bondeson, Y. Q. Liu, C. M. Fransson, B. Lennartson, C. Breitholtz, and T. S. Taylor, Nucl. Fusion **41**, 455 (2001).
[12]Y. Q. Liu, A. Bondeson, D. Gregoratto, C. M. Fransson, Y. Gribov, and R. Paccagnella, Nucl. Fusion **44**, 77 (2004).
[13]M. S. Chu and M. Okabayashi, Plasma Phys. Controlled Fusion **52**, 123001 (2010).
[14]Y. Q. Liu, M. S. Chu, W. F. Guo, F. Villone, R. Albanese, G. Ambrosino, M. Baruzzo, T. Bolzonella, I. T. Chapman, A. M. Garofalo, C. G. Gimblett, R. J. Hastie, T. C. Hender, G. L. Jackson, R. J. La Haye, M. J. Lanctot, Y. In, G. Marchiori, M. Okabayashi, R. Paccagnella, M. F. Palumbo, A. Pironti, H. Reimerdes, G. Rubinacci, A. Soppelsa, E. J. Strait, S. Ventre, and D. Yadykin, Plasma Phys. Controlled Fusion **52**, 104002 (2010).
[15]T. E. Evans, R. A. Moyer, K. H. Burrell, M. E. Fenstermacher, I. Joseph, A. W. Leonard, T. H. Osborne, G. D. Porter, M. J. Schaffer, P. B. Snyder, P. R. Thomas, J. G. Watkins, and W. P. West, Nat. Phys. **2**, 419 (2006).
[16]Y. Liang, H. R. Koslowski, P. R. Thomas, E. Nardon, B. Alper, P. Andrew, Y. Andrew, G. Arnoux, Y. Baranov, M. Bécoulet, M. Beurskens, T. Biewer, M. Bigi, K. Crombe, E. De La Luna, P. de Vries, W. Fundamenski, S. Gerasimov, C. Giroud, M. P. Gryaznevich, N. Hawkes, S. Hotchin, D. Howell, S. Jachmich, V. Kiptily, L. Moreira, V. Parail, S. D. Pinches, E. Rachlew, and O. Zimmermann, Phys. Rev. Lett. **98**, 265004 (2007).

[17]R. J. Hawryluk, D. J. Campbell, G. Janeschitz, P. R. Thomas, R. Albanese, R. Ambrosino, C. Bachmann, L. Baylor, M. Becoulet, I. Benfatto, J. Bialek, A. Boozer, A. Brooks, R. Budny, T. Casper, M. Cavinato, J.-J. Cordier, V. Chuyanov, E. Doyle, T. Evans, G. Federici, M. Fenstermacher, H. Fujieda, K. G'al1, A. Garofalo, L. Garzotti, D. Gates, Y. Gribov, P. Heitzenroeder, T. C. Hender, N. Holtkamp, D. Humphreys, I. Hutchinson, K. Ioki, J. Johner, G. Johnson, Y. Kamada, A. Kavin, C. Kesse, R. Khayrutdinov, G. Kramer, A. Kukushkin, K. Lackner, I. Landman, P. Lang, Y. Liang, J. Linke, B. Lipschultz, A. Loarte, G. D. Loesser, C. Lowry, T. Luce, V. Lukash, S. Maruyama, M. Mattei, J. Menard, M. Merola, A. Mineev, N. Mitchell, E. Nardon, R. Nazikian, B. Nelson, C. Neumeyer, J.-K. Park, R. Pearce, R. A. Pitts, A. Polevoi, A. Portone, M. Okabayashi, P. H. Rebut, V. Riccardo, J. Roth, S. Sabbagh, G. Saibene, G. Sannazzaro, M. Schaffer, M. Shimada, A. Sen, A. Sips, C. H. Skinner, P. Snyder, R. Stambaugh, E. Strait, M. Sugihara, E. Tsitrone, J. Urano, M. Valovic, M. Wade, J. Wesley, R. White, D. G. Whyte, S. Wu, M. Wykes, and L. Zakharov, Nucl. Fusion **49**, 065012 (2009).
[18]A. Kirk, E. Nardon, R. Akers, M. Bécoulet, G. De Temmerman, B. Dudson, B. Hnat, Y. Q. Liu, R. Martin, P. Tamain, D. Taylor, and MAST Team, Nucl. Fusion **50**, 034008 (2010).
[19]W. Suttrop, T. Eich, J. C. Fuchs, S. Günter, A. Janzer, A. Herrmann, A. Kallenbach, P. T. Lang, T. Lunt, M. Maraschek, R. M. McDermott, A. Mlynek, T. Pütterich, M. Rott, T. Vierle, E. Wolfrum, Q. Yu, I. Zammuto, H. Zohm, and ASDEX Upgrade Team, Phys. Rev. Lett. **106**, 225004 (2011).
[20]Y. M. Jeon, J.-K. Park, S. W. Yoon, W. H. Ko, S. G. Lee, K. D. Lee, G. S. Yun, Y. U. Nam, W. C. Kim, J.-G. Kwak, K. S. Lee, H. K. Kim, H. L. Yang, and KSTAR Team, Phys. Rev. Lett. **109**, 035004 (2012).
[21]Y. Sun, Y. Liang, Y. Q. Liu, S. Gu1, X. Yang, W. Guo, T. Shi, M. Jia, L. Wang, B. Lyu, C. Zhou, A. Liu, Q. Zang, H. Liu, N. Chu, H. H. Wang, T. Zhang, J. Qian, L. Xu, K. He, D. Chen, B. Shen, X. Gong, X. Ji, S. Wang, M. Qi, Y. Song, Q. Yuan, Z. Sheng, G. Gao, P. Fu, and B. Wan, Phys. Rev. Lett. **117**, 115001 (2016).
[22]R. Fitzpatrick, Phys. Plasmas **25**, 112505 (2018).
[23]R. Fitzpatrick, Phys. Plasmas **5**, 3325 (1998).
[24]A. Cole and R. Fitzpatrick, Phys. Plasmas **13**, 032503 (2006).
[25]F. L. Waelbroeck, I. Joseph, E. Nardon, M. Bécoulet, and R. Fitzpatrick, Nucl. Fusion **52**, 074004 (2012).
[26]Y. Q. Liu, A. Kirk, and E. Nardon, Phys. Plasmas **17**, 122502 (2010).
[27]Y. Q. Liu, A. Kirk, Y. Gribov, M. P. Gryaznevich, T. C. Hender, and E. Nardon, Nucl. Fusion **51**, 083002 (2011).
[28]N. M. Ferraro, Phys. Plasmas **19**, 056105 (2012).
[29]A. D. Turnbull, N. M. Ferraro, V. A. Izzo, E. A. Lazarus, J.-K. Park, W. A. Cooper, S. P. Hirshman, L. L. Lao, M. J. Lanctot, S. Lazerson, Y. Q. Liu, A. Reiman, and F. Turco, Phys. Plasmas **20**, 056114 (2013).
[30]S. R. Haskey, M. J. Lanctot, Y. Q. Liu, J. M. Hanson, B. D. Blackwell, and R. Nazikian, Plasma Phys. Controlled Fusion **56**, 035005 (2014).
[31]J. D. King, E. J. Strait, R. Nazikian, C. Paz-Soldan, D. Eldon, M. E. Fenstermacher, N. M. Ferraro, J. M. Hanson, S. R. Haskey, R. J. La Haye, M. J. Lanctot, S. A. Lazerson, N. C. Logan, Y. Q. Liu, M. Okabayashi, J.-K. Park, D. Shiraki, and A. D. Turnbull, Phys. Plasmas **22**, 112502 (2015).
[32]R. J. Buttery, S. Gerhardt, R. J. La Haye, Y. Q. Liu, H. Reimerdes, S. Sabbagh, M. S. Chu, T. H. Osborne, J.-K. Park, R. I. Pinsker, E. J. Strait, J. H. Yu, and DIII-D and NSTX Teams, Nucl. Fusion **51**, 073016 (2011).
[33]S. R. Haskey, M. J. Lanctot, Y. Q. Liu, C. Paz-Soldan, J. D. King, B. D. Blackwell, and O. Schmitz, Plasma Phys. Controlled Fusion **57**, 025015 (2015).
[34]R. A. Moyer, C. Paz-Soldan, R. Nazikian, D. M. Orlov, N. M. Ferraro, B. A. Grierson, M. Knölker, B. C. Lyons, G. R. McKee, T. H. Osborne, T. L. Rhodes, O. Meneghini, S. Smith, T. E. Evans, M. E. Fenstermacher, R. J. Groebner, J. M. Hanson, R. J. La Haye, T. C. Luce, S. Mordijck, W. M. Solomon, F. Turco, Z. Yan, L. Zeng, and DIII-D Team, Phys. Plasmas **24**, 102501 (2017).
[35]J. M. Hanson, F. Turco, T. C. Luce, G. A. Navratil, and E. J. Strait, Phys. Plasmas **28**, 042502 (2021).
[36]M. F. Heyn, I. B. Ivanov, S. V. Kasilov, W. Kernbichler, I. Joseph, R. A. Moyer, and A. M. Runov, Nucl. Fusion **48**, 024005 (2008).
[37]M. Bécoulet, G. Huysmans, X. Garbet, E. Nardon, D. Howell, A. Garofalo, M. Schaffer, T. Evans, K. Shaing, A. Cole, J.-K. Park, and P. Cahyna, Nucl. Fusion **49**, 085011 (2009).
[38]Y. Q. Liu, J. W. Connor, S. C. Cowley, C. J. Ham, R. J. Hastie, and T. C. Hender, Phys. Plasmas **19**, 072509 (2012).
[39]L. Li, Y. Q. Liu, Y. Liang, N. Wang, Q. Luan, F. C. Zhong, and Y. Liu, Nucl. Fusion **56**, 092008 (2016).
[40]L. Li, Y. Q. Liu, A. Loarte, O. Schmitz, Y. Liang, and F. C. Zhong, Phys. Plasmas **25**, 082512 (2018).
[41]A. H. Glasser, J. M. Greene, and J. L. Johnson, Phys. Fluids **18**, 875 (1975).
[42]K. Crombé, Y. Andrew, M. Brix, C. Giroud, S. Hacquin, N. C. Hawkes, A. Murari, M. F. F. Nave, J. Ongena, V. Parail, G. van Oost, I. Voitsekhovitch, and K.-D. Zastrow, Phys. Rev. Lett. **95**, 155003 (2005).
[43]T. Tala, Y. Andrew, K. Crombé, P. C. de Vries, X. Garbet, N. Hawkes, H. Nordman, K. Rantamäki, P. Strand, A. Thyagaraja, J. Weiland, E. Asp, Y. Baranov, C. Challis, G. Corrigan, A. Eriksson, C. Giroud, M.-D. Hua, I. Jenkins, H. C. M. Knoops, X. Litaudon, P. Mantica, V. Naulin, V. Parail, K.-D. Zastrow, and Contributors JET-EFDA, Nucl. Fusion **47**, 1012 (2007).
[44]W. M. Stacey and R. J. Groebner, Phys. Plasmas **15**, 012503 (2008).
[45]K. Kamiya, K. Ida, Y. Sakamoto, G. Matsunaga, A. Kojima, H. Urano, N. Oyama, Y. Koide, and Y. Kamada, Phys. Rev. Lett. **105**, 045004 (2010).
[46]W. Suttrop, A. Kirk, V. Bobkov, M. Cavedon, M. Dunne, R. M. McDermott, H. Meyer, R. Nazikian, C. Paz-Soldan, D. A. Ryan, E. Viezzer, M. Willensdorfer, ASDEX Upgrade, and MST1 Teams, Nucl. Fusion **58**, 096031 (2018).
[47]N. Aiba, J. Shiraishi, and S. Tokuda, Phys. Plasmas **18**, 022503 (2011).
[48]G. L. Xia, Y. Q. Liu, L. Li, C. J. Ham, Z. R. Wang, and S. Wang, Nucl. Fusion **59**, 126035 (2019).
[49]O. Schmitz, M. Becoulet, P. Cahyna, T. E. Evans, Y. Feng, H. Frerichs, A. Loarte, R. A. Pitts, D. Reiser, M. E. Fenstermacher, D. Harting, A. Kirschner, A. Kukushkin, T. Lunt, G. Saibene, D. Reiter, U. Samm, and S. Wiesen, Nucl. Fusion **56**, 066008 (2016).
[50]X. Bai, Y. Q. Liu, and Z. Gao, Phys. Plasmas **24**, 102505 (2017).
[51]L. Li, Y. Q. Liu, N. Wang, F. C. Zhong, Q. Luan, and Y. Wang, Nucl. Fusion **57**, 126027 (2017).
[52]X. Bai, Y. Q. Liu, and G. Z. Hao, Nucl. Fusion **61**, 066016 (2021).
[53]D. Gregoratto, A. Bondeson, M. S. Chu, and A. M. Garofalo, Plasma Phys. Controlled Fusion **43**, 1425 (2001).
[54]H. He, Y. Liu, J. Q. Dong, G. Z. Hao, T. Wu, Z. He, and K. Zhao, Nucl. Fusion **56**, 054003 (2016).